Photothermal AFM-IR Analysis of High Extinction Coefficient Materials: A Case Study with Silica and Silicate Glasses

Yen-Ting Lin[a], Hongtu He[a,b], Huseyin Kaya[c], Hongshen Liu[a], Dien Ngo[a], Nicholas J. Smith[d], Joy Banerjee[d], Ali Borhan[a], & Seong H. Kim [a,c*]

[a] Department of Chemical Engineering and Materials Research Institute, The Pennsylvania State University, University Park, PA 16802, United States

[b] Key Laboratory of Testing Technology for Manufacturing Process, Ministry of Education, Southwest University of Science and Technology, Mianyang, Sichuan 621010, China

[c] Department of Material Science and Engineering, The Pennsylvania State University, University Park, PA 16802, United States

[d] Science & Technology Division, Corning Incorporated, Corning, NY 14831, United States

Key words: AFM-IR, photothermal detection, silicate, glass network vibrations

* Correspondence to: shk10@psu.edu

Abstract

Photothermal atomic force microscopy coupled with infrared spectroscopy (AFM-IR) brings significant value as a spatially-resolved surface analysis technique for disordered oxide materials such as glasses, but additional development and fundamental understanding of governing principles is needed to interpret AFM-IR spectra since the existing theory described for organic materials does not work for materials with high extinction coefficients for IR absorption. This paper describes theoretical calculation of a transient temperature profile inside the IR-absorbing material considering IR refraction at the interface as well as IR adsorption and heat transfer inside the sample. This calculation explains differences in peak positions and amplitudes of AFM-IR spectra from those of specular reflectance and extinction coefficient spectra. It also addresses the information depth of the AFM-IR characterization of bulk materials. AFM-IR applied to silica and silicate glass surfaces has demonstrated novel capability of characterizing sub-surface structural changes and surface heterogeneity due to mechanical stresses from physical contacts as well as chemical alterations manifested in surface layers through aqueous corrosion.

1. Introduction

The development of atomic force microscopy coupled with infrared spectroscopy (AFM-IR) based on the photothermal detection principle was a breakthrough in IR spectroscopic imaging with nanoscale image resolution, which is far beyond the conventional diffraction limit of the IR wavelength.[1] It is a hybrid technique that correlates the IR absorption by the sample with the local height change (Δh) detected with an AFM probe upon thermal expansion of the sample.[2-4] The photothermal AFM-IR is known as a versatile spectroscopic imaging technique that can be applied to a wide range of materials.[5-11] One common aspect of literature examples in which this technique was demonstrated successfully is that the extinction coefficient of sample, which is the imaginary part (k) of the complex refractive index ($n + ik$), is relatively small and they are often deposited as a thin film on a substrate that does not absorb IR radiation.

In the photothermal AFM-IR theory derived by Dazzi et al.[3], the absorbed IR power (P_{abs}) is described as:

$$P_{abs}(\lambda) = \frac{2\pi}{\lambda} c\varepsilon_0 \frac{9\, k(\lambda)\, n(\lambda)}{(n(\lambda)^2 + 2)^2} |E_{inc}|^2 V \qquad (1)$$

where λ is the wavelength of IR light, c is the speed of light, ε_0 is the vacuum permittivity, $n(\lambda)$ and $k(\lambda)$ are the real and imaginary parts of complex refractive index at λ, respectively, E_{inc} is the electric field of the incident IR, and V is the sample volume within which absorption takes place. For most organics which have relatively small $k(\lambda)$ compared to $n(\lambda)$, $n(\lambda)$ does not vary drastically over the absorption band. Then, after normalization with the input IR power, $P_{abs}(\lambda)$ can be approximated to be proportional to $k(\lambda)$:[3]

$$P_{abs}(\lambda) \propto \frac{n\, k(\lambda)}{\lambda (n^2 + 2)^2} \qquad (2)$$

Through mathematical derivations solving the Fourier heat equation with the thermal diffusivity (α) and thermal conductivity (κ) of the sample and multiplying the temperature change with the coefficient of thermal expansion (CTE), Dazzi et al. have shown that $\Delta h(\lambda)$ is proportional to $k(\lambda)$.[3] For such systems, AFM-IR generates a spectrum that closely resembles the transmission absorption spectrum of the sample.[12]

This theory, however, cannot be applied to AFM-IR analysis of strongly IR absorbing modes of high-k materials such as oxide glasses. Due to the Kramers-Kronig relationship, $n(\lambda)$

also varies drastically in the strong absorption band region. As an example, Figure 1 compares the complex refractive index, $n(\lambda)$ and $k(\lambda)$,[13] and AFM-IR spectrum of fused quartz as well as $P_{abs}(\lambda)$ calculated from eq. (2). For comparison, the specular reflectance infrared (SR-IR) spectrum is also plotted. Although all spectra embody the vibrational responses of the same material upon absorption of the same IR, there are stark differences among the spectra. Neither the AFM-IR spectrum nor the $P_{abs}(\lambda)$ plot resembles the $k(\lambda)$ spectrum. Since the existing model fails to predict the AFM-IR spectra of highly absorbing materials, interpretations of AFM-IR spectral feature require more rigorous theoretical processing.

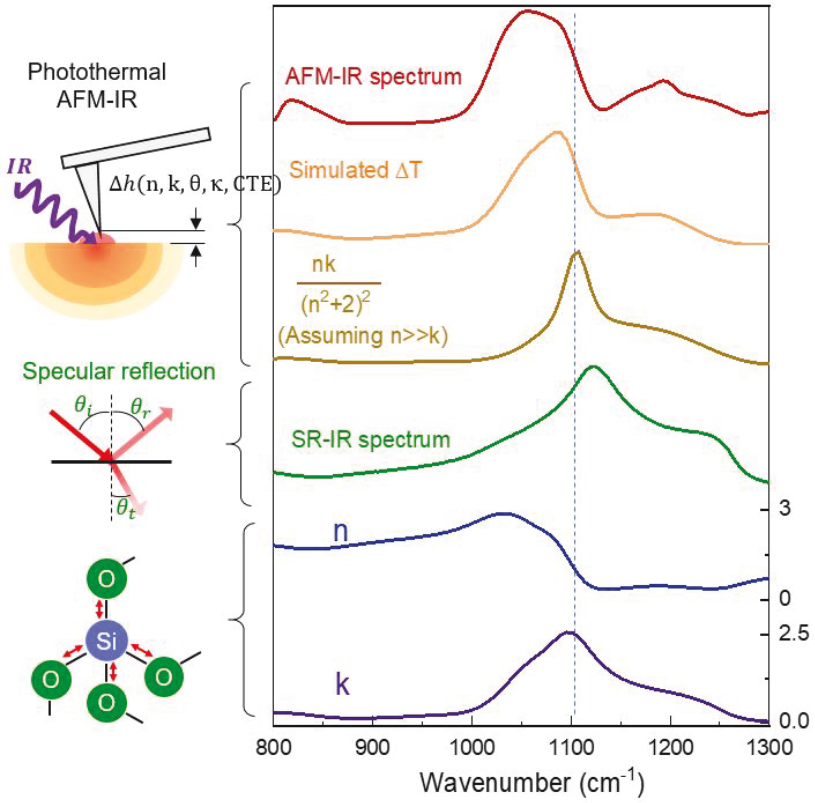

Figure 1. Comparison of complex refractive index (n, k),[13] SR-IR and AFM-IR spectra of fused quartz. The spectrum predicted using eq.(2) derived by Dazzi et al.[3] and the temperature change (ΔT) calculated in this work are also shown for comparison. Details of the SR-IR and AFM-IR data collection and the ΔT calculation are described in Sections 2.2 and 2.3, respectively.

Moreover, Eq.(1) is based on the electric dipole approximation in which the sample size is assumed to be much smaller than the IR wavelength.[3] Thus, the previous theory cannot address

the probe depth question of AFM-IR. Since $k(\lambda)$ of the vibrational modes of oxide glasses are large, the penetration or attenuation depth of IR inside the sample also varies substantially. This affects the probe depth at a given λ. Moreover, the AFM-IR signal intensity, $\Delta h(\lambda)$, arises as a convoluted outcome of multiple parameters including complex refractive index of the sample, the IR incident angle, IR attenuation in the sample,[14] as well as the thermal properties of the sample (α, κ, and CTE). The convoluted spectral features make the vibrational bands in AFM-IR spectra distinctly different from those of reflective and transmission IR spectra, as highlighted in Figure 1. This paper addresses the convoluted effects of these parameters in AFM-IR analysis of the network vibrations of various types of silicate glasses. Applications of AFM-IR characterization to spectroscopic analysis of glass surfaces subjected to mechanical indentation,[15] frictional wear,[16] and aqueous corrosion[17-18] are also discussed.

2. Experimental Details and Theoretical Calculation

2.1 2.1 AFM-IR and SR-IR experiments

Commercially available silica (fused quartz), silicate (soda lime silicate, SLS), borosilicate (Schott Zerodur®), boroaluminosilicate (Corning® Eagle XG® and international simple glass, ISG[19]) glasses were used. Nano-indentation and scratch marks on fused quartz and aqueous corrosion layer on ISG[20] were analyzed with AFM-IR. Polystyrene films deposited on fused quartz and silicon wafer were also analyzed for comparison. AFM-IR analysis was performed with a NanoIR3 system (Bruker) using a gold-coated silicon nitride probe (0.07-0.4 N m^{-1} spring constant, 13 ± 4 kHz resonant frequency, Bruker) in a contact scan mode. SR-IR spectra of glasses were measured by using a Bruker Vertex 80 FTIR spectrometer combined with a Hyperion 3000 FTIR microscope. Details of sample preparations as well as measurements conditions are in the Supporting Information (SI).

2.2 Theoretical calculation of local temperature rise under AFM-IR condition

There are several modes of operating AFM-IR to detect the small $\Delta h(\lambda)$ responses of the sample.[4] All modes are based on the local height change caused by oscillatory temperature fluctuation (ΔT), which can be modeled as a series of the ΔT profile by each IR laser pulse arriving at a set repetition rate. Once the ΔT profile of a single pulse is obtained, $\Delta h(\lambda)$ can be approximated by multiplying CTE to the average temperature change per pulse.[12] Figure 2 describes the

experimental geometry of AFM-IR and the axisymmetric model used for theoretical ΔT calculation.

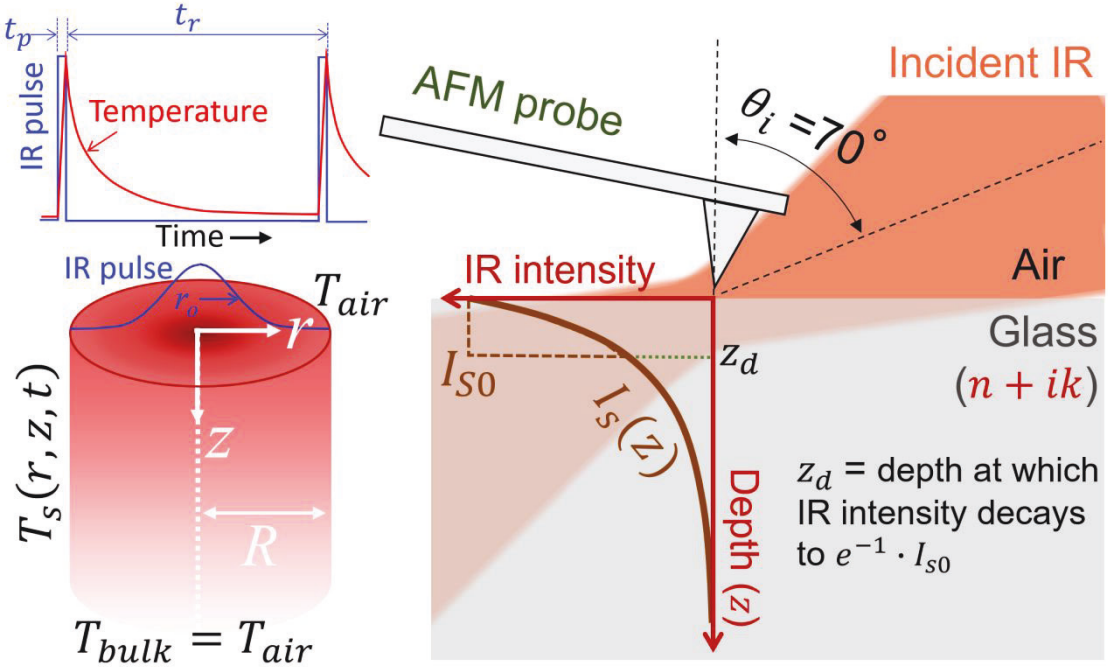

Figure 2. Schematic of AFM-IR experiment. The narrow-band IR pulse with a temporal pulse width t_p and a repetition time t_r is focused from the side of the AFM probe with an elliptical reflection mirror. The incidence angle (θ_i) defined by the center axis of the focused beam and the surface normal direction is 70°. Since most IR power delivered to the sample is confined within the area that is defined by three times the Gaussian beam radius (r_o), we consider a cylinder with a radius $R = 3r_o$. In our experimental setup, $r_o \approx 50$ μm. The model assumes that the temperature profile decays to the bulk temperature at the boundary of the cylinder.

First, the fraction of the irradiated IR going into the sample is estimated to be $(1 - R_i)$, where R_i is the reflectance of IR at the air / sample interface at the experimental incidence angle ($\theta_i = 70°$) which can be calculated with the Fresnel coefficient equations and the complex refractive index of the sample $(n + ik)$.[21] The IR beam propagating inside the sample is attenuated due to absorption. The characteristic attenuation length (z_d), at which the electric field of IR decreases to 36.7% (e^{-1}) of its original magnitude, is calculated using the extinction coefficient (Figure S1a). Assuming the absorbed IR energy to be the heat source, the rate of thermal energy generation per unit volume of the sample can be written as:

$$s(r,z,t) = s_{max} e^{\left[-\frac{z}{z_d} - \left(\frac{r}{r_0}\right)^2\right]} \delta(t) \;\; ; \;\; s_{max} = \frac{E_{input}(1 - R_i)}{\pi r_o^2 z_d} \qquad (3)$$

where E_{input} is the energy of each IR pulse, which is the input power (W) times the pulse repetition time (t_r), and the irradiated volume of the sample is approximated as $\pi r_o^2 z_d$. Note that R_i and z_d are functions of λ (Figure S1a). Using the characteristic scale R for length, R^2/α for time, and $R^2 s_{max}/\kappa$ for temperature difference (where a and κ are the thermal diffusivity and conductivity of the sample, respectively), the dimensionless equations governing the temperature distribution in the semi-infinite cylinder of radius R (bounded by a plane at $z = 0$) are given by:

$$\frac{\partial\theta}{\partial t} = \frac{1}{r}\frac{\partial}{\partial r}r\frac{\partial\theta}{\partial r} + \frac{\partial^2\theta}{\partial z^2} + S(r,z,t) \quad (4)$$

$$\theta(1,z,t) = 0\ ;\ \left.\frac{\partial\theta}{\partial z}\right|_{z=0} = Bi\theta(r,0,t)\ ;\ \left.\frac{\partial\theta}{\partial z}\right|_{z\to\infty} = 0\ ;\ \theta(r,z,0) = 0 \quad (5)$$

where $\theta = \kappa(T_S - T_{air})/R^2 s_{max}$ is the dimensionless temperature, all independent variables are dimensionless, $S = s(r^*, z^*, t^*)/s_{max}$, and $Bi = h_c R/\kappa$ is the Biot number (with h_c denoting the convective heat transfer coefficient).

In this calculation, a and κ of silica will be used, which are 8.3×10^{-7} m^2s^{-1} and 1.4 $Wm^{-1}K^{-1}$, respectively. The incident IR beam is assumed *p*-polarized for calculation of R_i in Eq. (3). Since the length scale of the system under consideration (R=150 μm) is small, Bi is on the order of 10^{-3} for a typical value of h_c = 10 $Wm^{-2}K^{-1}$ in air. In addition, the laser pulse duration (t_p = 100 ns) is much shorter than the thermal diffusion time in the system ($R^2/\alpha \approx 100$ ms). Thus, the location of the maximum temperature at the end of each pulse must be at the sample surface. This surface temperature (T_{S0}) can be estimated by neglecting thermal diffusion in Eq. (2) and integrating over a laser pulse duration to yield:

$$T_{S0} = T_{air} + \left[\frac{E_{input}(1-R_i)\alpha}{\pi r_o^2 z_d \kappa}\right] e^{-9r^2} \quad (6)$$

These equations are solved to calculate the spatial and temporal temperature profiles inside the sample after heating by the IR pulse (see SI). For extremely small Biot numbers (i.e., convective heat loss to air is negligible compared to heat conduction to the bulk), the temperature distribution within the sample (eq. S8-S10 in SI) can be expressed as:

$$\theta(r,z,t) = e^{t/z_d^2}\left[e^{\frac{z}{z_d}}\,\mathrm{erfc}\left(\frac{\sqrt{t}}{z_d} + \frac{z}{2\sqrt{t}}\right) + e^{\frac{-z}{z_d}}\mathrm{erfc}\left(\frac{\sqrt{t}}{z_d} - \frac{z}{2\sqrt{t}}\right)\right]\sum_{n=0}^{\infty}\frac{f(\beta_n)}{J_1^2(\beta_n)}J_0(\beta_n r)e^{-\beta_n^2 t} \quad (7)$$

3. Results and Discussion

3.1 Temperature profile calculated for irradiation with a single IR pulse

Figures 3a and 3b displays the temperature profiles inside the fused quartz sample irradiated with a 1100 cm^{-1} IR beam with a 2 mW power and a 100 ns pulse width. For comparison, we also calculated the temperature profiles inside a polystyrene sample irradiated with a 1452 cm^{-1} IR beam with the same power and pulse width, which are shown in Figures S2. At the end of the IR pulse, the surface temperature at the center of the Gaussian beam, $T_S(r = 0, z = 0, t = t_p)$, increases by ~6 K for the fused quartz surface (Figure 3a). In the polystyrene case, the temperature rise is calculated to ~0.4 K (Figure S2a). The system temperature exponentially decays and becomes close to the ambient temperature at a depth of $\sim 3 \times z_d$.

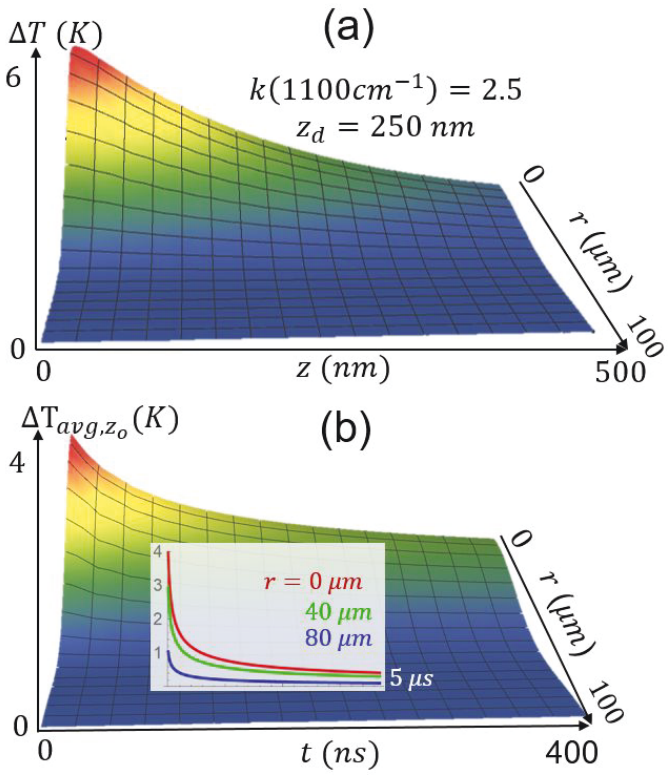

Figure 3. (a) Radial and depth distribution of temperature inside the fused quartz irradiated with a 1100 cm^{-1} pulse (2 mW) for t_p = 100 ns and (b) temporal decay of temperature inside the fused quartz (averaged over z_d). The inset plots the temperature decay over the repetition time at three locations from the center of the beam. The calculation results of a polystyrene sample are also shown in Figure S2 for comparison.

Figures 3b plots the average temperature rise over z_d, $\Delta T_{avg}(r,t) = \frac{1}{z_d}\int_0^{z_d} T_S(r,z,t)dz$, for the first 400 ns; the insets show the ΔT_{avg} change over the entire duration of the repetition time between laser pulses (t_r = 5 μs at a 200 kHz repetition). The temperature of fused quartz decreases fast after the pulse because the temperature gradient is large; but it does not decrease completely to the initial temperature before the next pulse comes. This means that the temperature of the irradiated region will gradually increase to a steady state value that will be determined by heat loss to the surrounding area beyond the boundary of the cylinder considered in this calculation (Figure 2). In AFM-IR experiment, the oscillatory height change matching with the repetition rate is detected with a lock-in-amplifier.

3.2 Comparison of AFM-IR spectra and calculated temperature profile of fused quartz

Figure 4 compares the experimental AFM-IR spectra of fused quartz collected at various locations within the irradiated area and the average temperature change over z_d by a single IR pulse, $\Delta T_{avg}(r,t_p)$, at the center, r_o, and $2r_o$ of the Gaussian beam profile. The agreement between the shape and relative intensity of the AFM-IR spectra and the $\Delta T_{avg}(r,t_p)$ profiles are quite reasonable. This supports the main thesis of AFM-IR that the height change detected by AFM is due to thermal expansion caused by local temperature change inside the sample upon IR absorption.

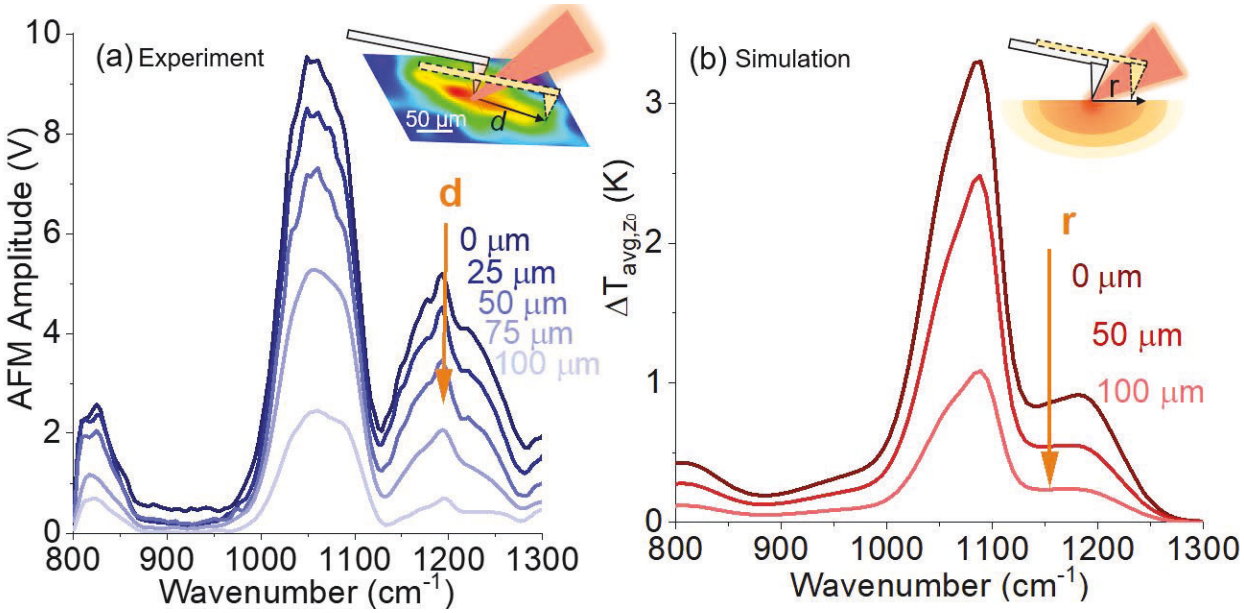

Figure 4. (a) AFM-IR spectra of fused quartz collected at locations with varying distances from the laser focal point. The inset image with a color scale shows the AFM-IR amplitude change over a 200 μm × 200 μm area. The AFM probe is displaced by the distance shown in the figure (d_1) along the IR irradiation direction. (b) Local average temperature, $\Delta T_{avg}(r,t_p)$, inside fused quartz as a function of IR wavenumber at r = 0 nm, 50 μm, and 100 μm at a 70° incidence angle. The IR pulse power in the calculation is 2 mW, which is the average power of IR laser pulses also used in the experiment. The calculation results for 50° and 60° incidence angles are shown in Figure S1b.

There are some discrepancies between the experimental AFM-IR spectra and the theoretical ΔT_{avg} spectra. In Section 2.3, the absorbed IR energy is assumed to heat the sample with a constant efficiency, regardless of vibrational modes. This might be an oversimplification. The different vibrational modes of amorphous silica network may have different contributions to thermal conductivity of the sample.[22-23] So, the temperature increase per absorbed IR energy may vary depending on how the excited vibrational mode dissipates the absorbed photon energy to the surrounding. Also, the calculation is done for a constant θ_i which is set to 70° (based on the specification of the instrument provided by Bruker). But in experiment, the IR incidence angle varies over a broad range because the beam is focused from a large elliptical reflection mirror (Figure 2). As the incidence angle decreases, the transmittance $(1 - R_i)$ near the 1200 cm^{-1} region increases significantly, while that near the 1100 cm^{-1} main band remains relatively constant (Figure S1a). Thus, the smaller incidence angle portion of the beam will greatly enhance the AFM-IR signal intensity around 1200 cm^{-1} (see the example for $\theta_i = 50°, 60°,$ and $70°$ in Figure S1b). Also, any reflection of the IR beam by the gold-coated cantilever will be near surface normal direction and thus amplify this incidence angle effect. The features near 820 and 1200 cm^{-1} in Figure 4 (a) look larger as compared to the same bands in Figure 4 (b). It might be possible that the 1060 cm^{-1} main band in AFM-IR is nearly saturated because the optical attenuation depth is smaller than the thermal diffusion length.

3.3 AFM-IR spectra of multicomponent silicate glasses

Figure 5a compares the AFM-IR spectra, SR-IR spectra, and extinction coefficient $k(\lambda)$ of various multicomponent silicate glasses as well as fused quartz (type-I silica).[24] The vibrational bands around 1050 – 1100 cm^{-1} in the $k(\lambda)$ spectra of silica and silicate glasses are attributed to the asymmetric stretch of Si-O bonds in the network.[25-26] In the SR-IR spectra, the Si-O stretch band appears slightly blue-shifted compared to the $k(\lambda)$ spectra. This is because $n(\lambda)$ is smaller

in the higher wavenumber side of the absorption band (Figure 1), so that the reflectance (R_i) is enhanced in that region.[25, 27] In the AFM-IR amplitude spectra, however, the main Si-O stretch band is slightly red-shifted as compared to the $k(\lambda)$ spectra. This could be attributed to the fact that the transmittance $(1 - R_i)$ is enhanced in the lower wavenumber side of the absorption band (Figure S1a).

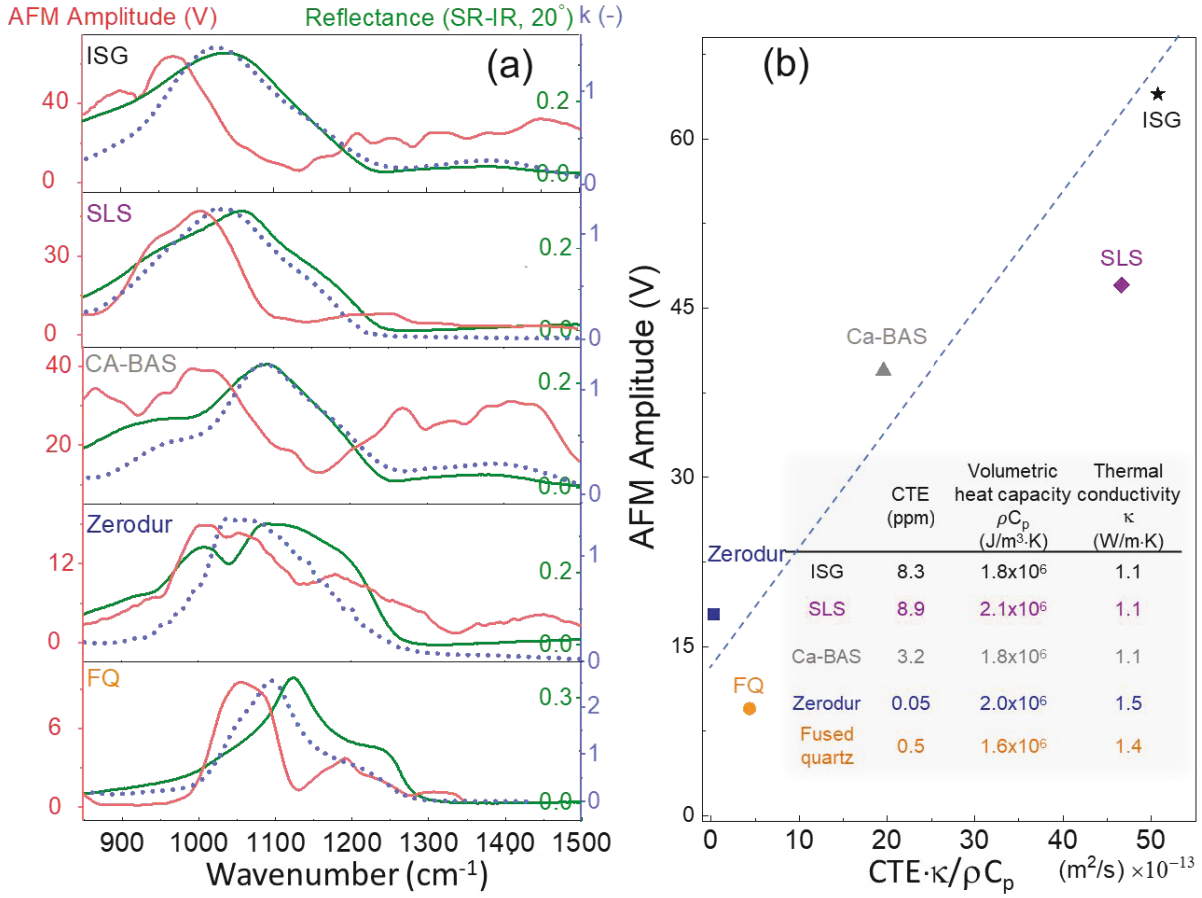

Figure 5. (a) AFM-IR amplitude spectra (red; left scale), SR-IR spectra (green; right inside scale), and extinction coefficient (blue dots; right outside scale) of ISG, SLS, Ca-BAS, Zerodur®, and fused quartz. (b) Comparison of the CTE/($\rho C_p \cdot \kappa$) magnitude and the AFM-IR amplitude of the glass studied.

In the case of borosilicate and boroaluminosilicate glasses, the weak bands around 1400 cm^{-1} in the $k(\lambda)$ spectra are ascribed to the B-O stretch of the three-coordinated BO_3 unit in the glass.[28-29] The four-coordinated boron species are expected to appear as a weak band around ~900 cm^{-1},[30-32] which often overlaps with the Si-O stretch mode involving nonbridging oxygen groups.[25] The intensities of these bands in the SR-IR spectra of ISG and Ca-BAS, which do not have

nonbridging Si-O bonds, are significantly larger than those in the $k(\lambda)$ spectra. At this moment, there is no good theoretical explanation for this observation; the only speculative explanation for this discrepancy could be the possibility that the conversion of the absorbed photon energy to heat might be more efficient for the B-O stretch mode than the Si-O stretch mode.[22-23]

In the spectral scanning mode of AFM-IR, the wavenumber of the irradiated IR pulse is changed stepwise while monitoring the height change at the AFM contact resonance frequency to which the IR pulse repetition rate is tuned. If the IR-induced thermal expansion of the sample is instantaneous and fully reversible (i.e., the response is fully elastic), then there would be no loss component in detection of the thermal expansion of the sample, and the phase difference between the thermal excitation (IR pulse) and the detected signal (AFM-IR amplitude) would be constant. However, the AFM-IR phase signal (Figure S3) varies as the IR wavenumber is scanned. There are many processes involved in detection of $\Delta h(\lambda)$. To name a few, they include the thermal dissipation of the absorbed IR photon energy, heat loss to the surrounding volume, propagation and accumulation of thermal expansion from the subsurface region to the surface, dynamic coupling of the surface height change to the lock-in detection of AFM, and so on.[12, 33-35] Unless all these parameters are known, it would be difficult to quantitatively interpret the phase signal of AFM-IR. In the case of Zerodur, the phase change is quite large over a very broad spectral range (Figure S3). Note that Zerodur is not a pure glass with a homogenous structure; it is a glass ceramic containing crystalline ceramic particles (~50 nm in diameter) with negative CTE dispersed in glass with positive CTE.[36] Maybe, this heterogeneity introduces additional loss processes in heat dissipation and thermal expansion, creating a large phase shift.

Even though all dynamic details cannot be fully captured, comparing the AFM-IR amplitude with thermal properties could provide a rule-of-thumb that might be useful for comparison of signal intensities of different materials. For the same amount of energy taken up by the material through IR absorption, the instantaneous or adiabatic temperature rise (during t_p) will be determined by the volumetric heat capacity, which is the product of density and specific heat capacity (ρC_p). During the repetition period (t_r), heat loss to the surrounding will occur. The faster heat loss is (i.e., larger κ), the larger the change will be in the temperature profile during the heat dissipation between pulses. Under the elastic response assumption, the height change for a given temperature change will be proportional to CTE. Thus, the amplitude of the cantilever deflection

signal will be large when the material CTE is large, heat dissipation is rapid (large κ), and the heat capacity is small. In Figure 5b, the AFM-IR amplitudes of the glasses analyzed in this study are compared with the magnitude of $CTE \cdot \kappa/\rho C_p$ as a figure of merit combining these thermal attributes.[24, 37-41] This plot shows that the maximum AFM-IR signal intensity scales roughly with thermal properties of the sample. Note that this comparison does not include the optical term, $(1 - R_i)$, which is a function of $n(\lambda)$, $k(\lambda)$, and θ_i.

3.4 Effective probe depth of AFM-IR analysis

Unlike other AFM-based vibrational spectroscopic imaging techniques such as tip-enhanced Raman spectroscopy (TERS) and nano-IR with scattering scanning near-field optical microscopy (s-SNOM) that detect only tens of nm deep from the surface,[42-43] the information depth of AFM-IR is much deeper. [44-47] Based on our temperature profile calculation, the heated zone is in the range of tens of microns for organics (Figure S2a); so, any discrimination of the signal from the deeper region must originate from convolution of the thermal expansion of the entire heated zone and its subsequent detection by the AFM cantilever.[4, 33, 48] In the case of network vibrations of glassy materials, the extinction coefficient in the absorbing region is quite high so that the heated zone is confined very close to the surface—especially at the IR wavelength close to the maximum absorption peak (Figure 3a). For a homogeneous solid (like glass) with high elastic modulus, the entire heated region will contribute to the topographic height change at the surface $\Delta h(\lambda)$. Based on this argument, the effective probe depth (or information depth) is expected to extend to two or three times of z_d. In the case of fused quartz, z_d varies from ~250 nm at 1100 cm^{-1} to 5 μm at 890 cm^{-1} (see Figure S1a).

For a layered system, the AFM-IR signal would be the convolution of all contributions from individual layers within the effective probe depth. Figure 6a displays AFM-IR spectra of polystyrene-coated fused quartz surfaces, as well as those of pristine fused quartz and a thick polystyrene film (~60 μm on a gold surface). Since polystyrene is a weak IR absorber, its AFM-IR spectrum is similar to the $k(\lambda)$ spectrum (Figure S4). The polystyrene-coated fused quartz spectra could be fitted by least squares regression using a linear combination of fused quartz and polystyrene spectra. As shown in Figure 6b, the contribution of the polystyrene film to the overall spectrum increases in proportion to the film thickness. Notably, however, the fitted contribution from the fused quartz (substrate) is relatively constant. Another experiment was conducted with

the polystyrene thin films on a silicon wafer and the same trend was observed (Figure S5). These results confirm that the AFM-IR signal is the sum of thermal expansion of all subsurface components within the IR attenuation depth.

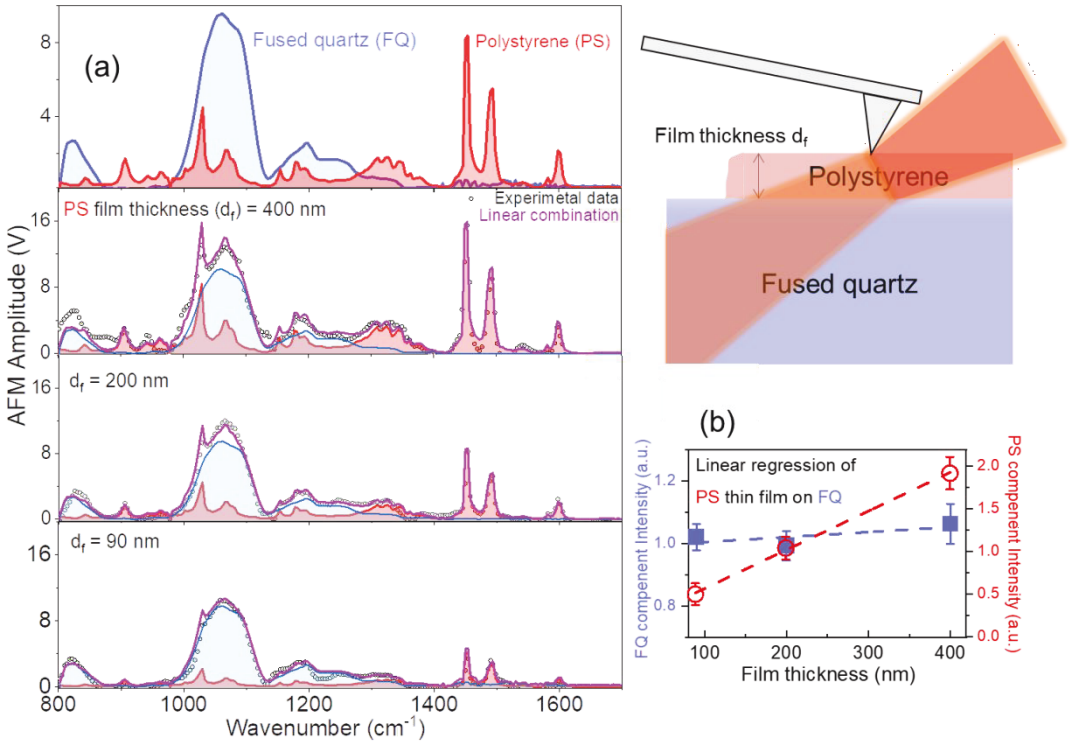

Figure 6. (a) AFM-IR spectra of pristine fused quartz (blue) and thick polystyrene film (red) and those of fused quartz surfaces coated with thin films of polystyrene with a thickness (d_f) of 90 nm, 200 nm, and 400 nm (open circles). In the panels of the 90 nm, 200 nm, and 400 nm thick polystyrene-coated fused quartz, the fit result from multi-component linear regression (pink) as well as the fused quartz (blue) and polystyrene film (red) components are also shown. (b) Least-squared linear regression result of the AFM-IR spectra of polystyrene-coated fused quartz. The thickness dependence of the polystyrene contribution is statistically significant ($p < 0.009$), while the changes in the fused quartz contribution is statistically insignificant ($p > 0.18$).

3.5 AFM-IR characterization of glass surface heterogeneity

Inhomogeneity of the glass surface and subsurface structure may have a huge impact on the chemical and mechanical durability of glass.[49-52] Therefore, it is important to characterize such defects with a high spatial resolution in both lateral and depth dimensions. AFM-IR provides a unique opportunity to perform vibrational spectroscopic analysis with excellent lateral resolution; the depth resolution would be determined by the optical and thermal properties of the material as

well as the detection mode.[35, 44, 53] Here, we present two examples from which the surface sensitivity and lateral resolution of AFM-IR can be gauged qualitatively.

Figure 7a shows the topographic image and line profile of a nanoindentation mark on a fused quartz surface made with a Berkovich tip, along with the AFM-IR amplitude spectra acquired both inside and outside of the indentation mark. It is well known that fused quartz undergoes densification upon indentation.[54-56] Previous studies have shown that subsurface densification induces elongation of the bridging Si-O bond length distribution, which manifests as a red-shift of the Si-O stretching band in IR spectra.[26, 57] In Figure 7a, the AFM-IR band between 1000 cm^{-1} and 1100 cm^{-1} is slightly red-shifted in the spectrum taken at the bottom of the indent (position-2) compared to that taken outside the indent (position-1). Upon annealing of the sample at a temperature 0.9 times glass transition temperature (T_g), the densification is fully reverted, and the surface topography is partially recovered.[58-59] The spectrum taken at the bottom of the annealed indent mark is almost identical to the reference spectrum taken from the un-indented outside region.

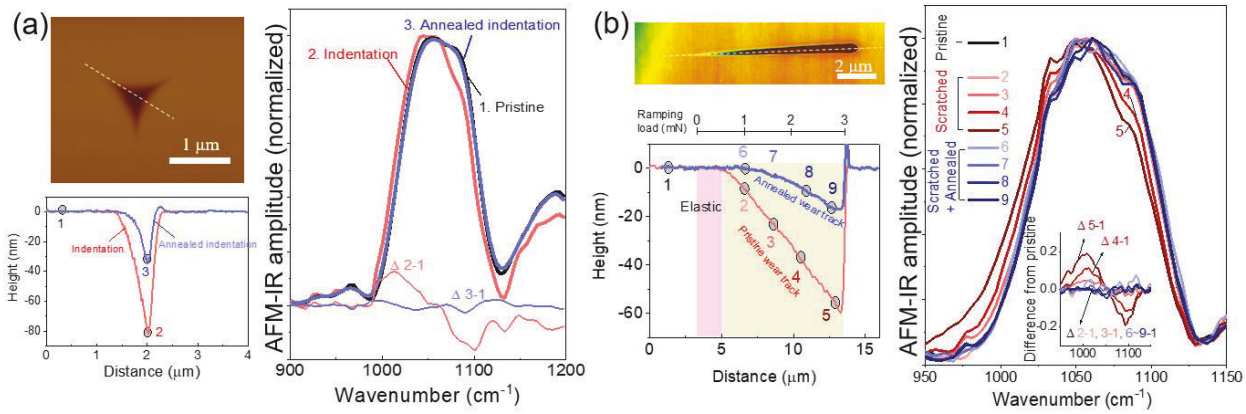

Figure 7. (a) Topography, line profile, and AFM-IR spectra of a nanoindent on fused quartz made with a Berkovich indenter at a 5 mN load. (b) Topography, line profile, and AFM-IR spectra of a nanoscratch on fused quartz made with a conospherical tip (radius = 150 nm) at a ramp load from 0 mN to 3 mN while sliding over a 10 μm distance. The same samples were analyzed before and after sub-T_g annealing. The differences (Δ) between local spectra are also shown.

Figure 7b show the AFM-IR analysis of a nanoscratch mark on fused quartz made with a conospherical tip translating at 1 μm/s while the load was ramped from 0 to 3 mN. Along the nanoscratch direction, the degree of red-shift in the AFM-IR amplitude peak gradually increases as the load increases (e.g., comparing positions 3 → 4 → 5). This is because the degree of subsurface densification increases with the applied load.[13,47] At position-2 where plastic

deformation is relatively small (thus, subsurface densification is minute), the red-shift of the Si-O stretch band is not readily discernable. This is in contrast to the s-SNOM-based nano-IR analysis result showing a noticeable red-shift in this same region.[15] Even in the elastic contact regime (pink region in Figure 7b), s-SNOM-based nano-IR was able to detect a very small red-shift.[15] The discrepancy between these photothermal-IR and s-SNOM-IR data can be explained by inherent differences in the probe depths of the two techniques. The s-SNOM method relies on the scattering of the evanescent field in the near field, so its probe depth is on the order of tens of nm.[15, 42] In contrast, the AFM-IR system relies on photothermal expansion. Since the IR attenuation by absorption takes place in the far field (which can be characterized by z_d, Figure 4a), the AFM-IR spectrum will have much larger contributions from the deeper region, implying much less surface sensitivity of the photothermal AFM-IR process compared to the s-SNOM process.

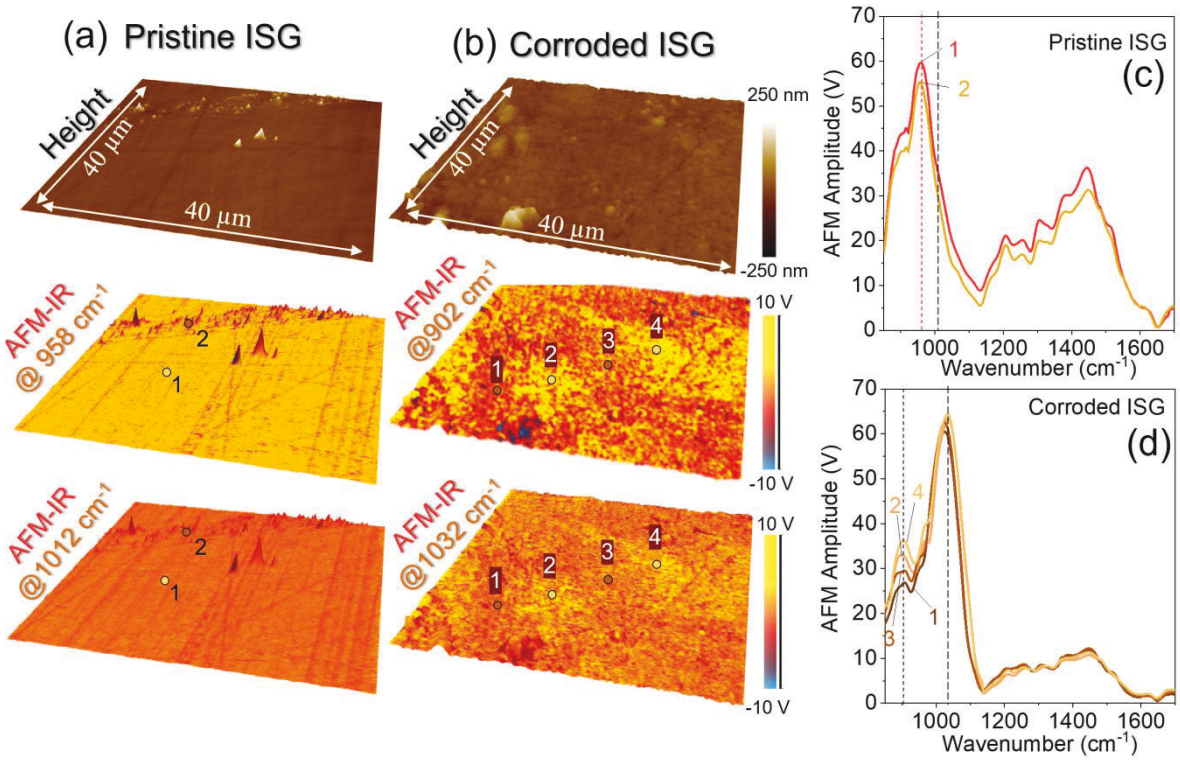

Figure 8. Topography and AFM-IR intensity map of (a) pristine and (b) corroded ISG surfaces. The wavenumber of the IR beam used in the mapping is shown in the left of each image. (c,d) AFM-IR spectra collected at various locations marked in the AFM-IR intensity map on (c) pristine and (b) corroded ISG surfaces. The corrosion was conducted in a pH 7 solution pre-saturated with soluble silica at 90 °C for 14 days.

Aqueous corrosion of glass can lead to alteration of the glass matrix and changes in glass network structure within a surface layer.[18, 20] In the case of ISG, a boroalumunosilicate glass studied as a model nuclear waste vitrification,[19] about 2 μm thick corrosion layer is formed within several days of immersion in silica-saturated aqueous solutions at pH 7, and this ultrathin layer can protect the glass from further corrosion for more than 20 years (which is the longest time tested so far).[20, 60] Figure 8 displays the topography and AFM-IR intensity images of pristine and 14-days corroded ISG glass surfaces, as well as their AFM-IR spectra. In the AFM-IR spectrum of pristine ISG (Figure 8c), the main peak at 958 cm^{-1} corresponds to the 1030 cm^{-1} peak in the $k(\lambda)$ and SR-IR spectra (see Section 3.3). The broad band in the 1300 – 1500 cm^{-1} region originates from the B-O stretch in the glass.[61] In the topography and AFM-IR intensity maps, some scratch marks and debris can be identified. The AFM-IR spectral features collected at such locations (for example, position-2 in Figure 8a) are almost identical to the spectra collected in flat regions, except for small differences in the overall intensities due to topographic artifacts (Figure 8c).[62] The convolution from topographic artifacts is further explained in the Supporting Information (Figure S6).

The corroded ISG surfaces (Figure 8d) show spectral features that are drastically different from the pristine samples. The decrease of the signal intensity in the 1300 – 1500 cm^{-1} region is due to the loss of boron species from the glass network.[29-30, 63] Although time-of-flight secondary ion mass spectrometry depth profiling showed that the boron is almost completely depleted in the corroded layer,[60, 64] AFM-IR still shows clearly discernable bands in the B-O stretch region. This comes from the boron species in the bulk below the ~2 μm thick boron-depleted layer, and again exemplifies the relative deep probe depth of AFM-IR in the weakly-absorbing spectral region. In the corroded ISG spectra, the ~958 cm^{-1} band is diminished, while the main band is blue-shifted to ~1032 cm^{-1}. This blueshift is interpreted as an indication of the transition to a "silica-like" network structure (Figure 5).[26, 65] The probe depth at this maximum intensity position of the Si-O stretch mode (Figure S1a) is smaller than the corrosion layer thickness.

Local inhomogeneity can be seen in the AFM-IR intensity maps of corroded ISG; this inhomogeneity does not correlate with the topographic height change (Figure 8b). Positions-1,3 show the major band at ~1022 cm^{-1} and a smaller band at ~900 cm^{-1}, while positions-2,4 have the main bands at 1032 cm^{-1} and a larger intensity at ~900 cm^{-1}. Considering that the AFM-IR peak position is red-shifted from the $k(\lambda)$ spectrum (Section 3.3), the ~900 cm^{-1} band can be putatively

ascribed to the vibrational modes involving non-bridging Si-O species, which normally appears as a shoulder band at ~950 cm^{-1} in SR-IR spectra. Alternatively, it could be due to differences in the population of four-coordinated boron species (Figure 5a) near the interface between the alteration layer and the bulk glass.[60] The finding of such local inhomogeneity in glass network structure of the aqueous-corroded surface layer is unprecedented. Its implication on the overall chemical durability and stability of the surface layer formed by aqueous corrosion has not been investigated and would be the subject of a future study.

4. Conclusion

This work examines the theory and application of the resonance-enhanced photothermal AFM-IR technique to materials that exhibit relatively strong absorption peaks in the mid-IR wavelength region, with a focus on silica and silicate glasses. These materials show very large extinction coefficients for the primary network vibration ($k(\lambda)$ >1) in comparison to organic materials, which invalidates some of the underlying assumptions that are commonly made when connecting the measured AFM-IR spectral response to the IR absorption behavior. These effects notably manifest in distortion of the AFM-IR spectra in comparison to the true absorption spectra. Modeling of the IR absorption and subsequent heating and cooling behavior of silica shows a large local temperature change and corresponding thermal gradients as a function of both time and distance from the focal spot during laser pulse. The subsequent impact to the measured signal could be verified across a variety of silicate glasses, and exemplifies the need to more holistically consider thermal properties (e.g., CTE, heat conductivity, heat capacity, etc.) of highly absorptive materials. Finally, we highlight in this work, through both experiment and modeling, the relatively deep information depth of AFM-IR (implying relatively low surface-sensitivity). Although this inherent limitation poses a challenge to reliably detect changes in glass structure in some instances of shallow surface modification, AFM-IR can still reasonably detect structural changes that occur under high-load diamond indentation or in relatively thick, corrosion-induced surface alteration layers.

Acknowledgments. This work was supported by National Science Foundation (Grant No. DMR-2011410) and supported as part of the Center for Performance and Design of Nuclear Waste Forms and Containers, an Energy Frontier Research Center funded by the U.S. Department of Energy, Office of Science, Basic Energy Sciences under Award # DE-SC0016584. YTL was supported by Corning Incorporated during the period of this research. The authors acknowledge the support from the Penn State Materials Characterization Laboratory (MCL) for the use of AFM-IR instrument. The authors also acknowledge the support from Timothy M. Gross for helping with the crucible melting of silicate glasses used in mechanochemical wear tests.

Supporting information: Experimental details, theoretical derivations and supplementary calculation and AFM-IR spectra.

5. References

1. Schlessinger, M., *Infrared technology fundamentals*. Routledge: 2019.
2. Hammiche, A.; Pollock, H.; Reading, M.; Claybourn, M.; Turner, P.; Jewkes, K., Photothermal FT-IR spectroscopy: A step towards FT-IR microscopy at a resolution better than the diffraction limit. *Appl. Spectrosc.* **1999,** *53* (7), 810-815.
3. Dazzi, A.; Glotin, F.; Carminati, R., Theory of infrared nanospectroscopy by photothermal induced resonance. *J. Appl. Phys.* **2010,** *107* (12), 124519.
4. Mathurin, J.; Deniset-Besseau, A.; Bazin, D.; Dartois, E.; Wagner, M.; Dazzi, A., Photothermal AFM-IR spectroscopy and imaging: Status, challenges, and trends. *J. Appl. Phys.* **2022,** *131* (1), 010901.
5. Liu, Y.; Zhang, B.; Xu, W.; Haibibu, A.; Han, Z.; Lu, W.; Bernholc, J.; Wang, Q., Chirality-induced relaxor properties in ferroelectric polymers. *Nat. Mater.* **2020,** *19* (11), 1169-1174.
6. Mikhalchan, A.; Banas, A. M.; Banas, K.; Borkowska, A. M.; Nowakowski, M.; Breese, M. B.; Kwiatek, W. M.; Paluszkiewicz, C.; Tay, T. E., Revealing chemical heterogeneity of CNT fiber nanocomposites via nanoscale chemical imaging. *Chem. Mater.* **2018,** *30* (6), 1856-1864.
7. Liu, Y.; Yang, T.; Zhang, B.; Williams, T.; Lin, Y. T.; Li, L.; Zhou, Y.; Lu, W.; Kim, S. H.; Chen, L. Q., Structural insight in the interfacial effect in ferroelectric polymer nanocomposites. *Adv. Mater.* **2020,** *32* (49), 2005431.
8. Yang, J.; Hatcherian, J.; Hackley, P. C.; Pomerantz, A. E., Nanoscale geochemical and geomechanical characterization of organic matter in shale. *Nat. Commun.* **2017,** *8* (1), 1-9.
9. Hassenkam, T.; Andersson, M. P.; Dalby, K. N.; Mackenzie, D.; Rosing, M. T., Elements of Eoarchean life trapped in mineral inclusions. *Nature* **2017,** *548* (7665), 78-81.
10. Farber, C.; Wang, R.; Chemelewski, R.; Mullet, J.; Kurouski, D., Nanoscale structural organization of plant epicuticular wax probed by atomic force microscope infrared spectroscopy. *Anal. Chem.* **2019,** *91* (3), 2472-2479.
11. Ruggeri, F.; Longo, G.; Faggiano, S.; Lipiec, E.; Pastore, A.; Dietler, G., Infrared nanospectroscopy characterization of oligomeric and fibrillar aggregates during amyloid formation. *Nat. Commun.* **2015,** *6* (1), 1-9.
12. Dazzi, A.; Prater, C. B., AFM-IR: Technology and applications in nanoscale infrared spectroscopy and chemical imaging. *Chem. Rev.* **2017,** *117* (7), 5146-5173.
13. Luo, J.; Smith, N. J.; Pantano, C. G.; Kim, S. H., Complex refractive index of silica, silicate, borosilicate, and boroaluminosilicate glasses–Analysis of glass network vibration modes with specular-reflection IR spectroscopy. *J. Non-Cryst. Solids* **2018,** *494*, 94-103.

14. Amma, S.; Luo, J. W.; Pantano, C. G.; Kim, S. H., Specular reflectance (SR) and attenuated total reflectance (ATR) infrared (IR) spectroscopy of transparent flat glass surfaces: A case study for soda lime float glass. *J. Non-Cryst. Solids* **2015,** *428*, 189-196.
15. He, H.; Chen, Z.; Lin, Y.-T.; Hahn, S. H.; Yu, J.; van Duin, A. C.; Gokus, T. D.; Rotkin, S. V.; Kim, S. H., Subsurface structural change of silica upon nanoscale physical contact: Chemical plasticity beyond topographic elasticity. *Acta Materialia* **2021,** *208*, 116694.
16. He, X.; Ngo, D.; Kim, S. H., Mechanochemical Reactions of Adsorbates at Tribological Interfaces: Tribopolymerizations of Allyl Alcohol Coadsorbed with Water on Silicon Oxide. *Langmuir* **2019,** *35* (48), 15451-15458.
17. Kaya, H.; Ngo, D.; Gin, S.; Kim, S. H., Spectral changes in Si–O–Si stretching band of porous glass network upon ingress of water. *J. Non-Cryst. Solids* **2020,** *527*, 119722.
18. Kaya, H.; Ngo, D.; Smith, N. J.; Gin, S.; Kim, S. H., Network structure in alteration layer of boroaluminosilicate glass formed by aqueous corrosion. *J. Non-Cryst. Solids* **2021,** *553*, 120494.
19. Gin, S.; Abdelouas, A.; Criscenti, L. J.; Ebert, W. L.; Ferrand, K.; Geisler, T.; Harrison, M. T.; Inagaki, Y.; Mitsui, S.; Mueller, K. T.; Marra, J. C.; Pantano, C. G.; Pierce, E. M.; Ryan, J. V.; Schofield, J. M.; Steefel, C. I.; Vienna, J. D., An international initiative on long-term behavior of high-level nuclear waste glass. *Mater. Today* **2013,** *16* (6), 243-248.
20. Gin, S.; Jollivet, P.; Fournier, M.; Angeli, F.; Frugier, P.; Charpentier, T., Origin and consequences of silicate glass passivation by surface layers. *Nat. Commun.* **2015,** *6* (1), 1-8.
21. Fujiwara, H., *Spectroscopic ellipsometry: principles and applications*. John Wiley & Sons: 2007.
22. Allen, P. B.; Feldman, J. L.; Fabian, J.; Wooten, F., Diffusons, locons and propagons: Character of atomic vibrations in amorphous Si. *Philos. Mag. B* **1999,** *79* (11-12), 1715-1731.
23. Lv, W.; Henry, A., Examining the validity of the phonon gas model in amorphous materials. *Sci. Rep.* **2016,** *6* (1), 1-8.
24. Brueckner, R., Properties and structure of vitreous silica. I. *J. Non-Cryst. Solids* **1970,** *5* (2), 123-175.
25. Liu, H.; Kaya, H.; Lin, Y. T.; Ogrinc, A.; Kim, S. H., Vibrational spectroscopy analysis of silica and silicate glass networks. *J. Am. Ceram. Soc.* **2021**.
26. Liu, H.; Hahn, S. H.; Ren, M.; Thiruvillamalai, M.; Gross, T. M.; Du, J.; van Duin, A. C.; Kim, S. H., Searching for correlations between vibrational spectral features and structural parameters of silicate glass network. *J. Am. Ceram. Soc.* **2020,** *103* (6), 3575-3589.
27. Amma, S.-i.; Luo, J.; Pantano, C. G.; Kim, S. H., Specular reflectance (SR) and attenuated total reflectance (ATR) infrared (IR) spectroscopy of transparent flat glass surfaces: A case study for soda lime float glass. *J. Non-Cryst. Solids* **2015,** *428*, 189-196.
28. Kamitsos, E., Infrared spectroscopy of glasses. *Modern Glass Characterization* **2015**, 1-42.
29. Möncke, D.; Dussauze, M.; Kamitsos, E.; Varsamis, C.; Ehrt, D., Thermal poling induced structural changes in sodium borosilicate glasses. *Phys. Chem. Glas.: Eur. J. Glass Sci. Technol. B* **2009,** *50* (3), 229-235.
30. Kamitsos, E., Infrared studies of borate glasses. *Phys. Chem. Glasses* **2003,** *44* (2), 79-87.
31. Konijnendijk, W. L.; Stevels, J. M., The structure of borate glasses studied by Raman scattering. *J. Non-Cryst. Solids* **1975,** *18* (3), 307-331.
32. Gautam, C.; Yadav, A. K.; Singh, A. K., A review on infrared spectroscopy of borate glasses with effects of different additives. *Int. Sch. Res. Notices* **2012,** *2012*.
33. Xiao, C.; Xin, X.; He, X.; Wang, H.; Chen, L.; Kim, S. H.; Qian, L., Surface Structure Dependence of Mechanochemical Etching: Scanning Probe-Based Nanolithography Study on Si(100), Si(110), and Si(111). *ACS Appl. Mater. Interfaces* **2019,** *11* (23), 20583-20588.
34. Barlow, D. E.; Biffinger, J. C.; Cockrell-Zugell, A. L.; Lo, M.; Kjoller, K.; Cook, D.; Lee, W. K.; Pehrsson, P. E.; Crookes-Goodson, W. J.; Hung, C.-S., The importance of correcting for variable probe–sample interactions in AFM-IR spectroscopy: AFM-IR of dried bacteria on a polyurethane film. *Analyst* **2016,** *141* (16), 4848-4854.

35. Morsch, S.; Lyon, S.; Edmondson, S.; Gibbon, S., Reflectance in AFM-IR: implications for interpretation and remote analysis of the buried interface. *Anal. Chem.* **2020,** *92* (12), 8117-8124.
36. AG, S., TIE-37: Thermal expansion of ZERODUR. *Schott Technical Paper* **2006**.
37. Kaspar, T. C.; Ryan, J. V.; Pantano, C. G.; Rice, J.; Trivelpiece, C.; Hyatt, N. C.; Corkhill, C. L.; Mann, C.; Hand, R. J.; Kirkham, M. A., Physical and optical properties of the International Simple Glass. *npj Mater. Degrad.* **2019,** *3* (1), 1-15.
38. Angeli, F.; Charpentier, T.; Jollivet, P.; de Ligny, D.; Bergler, M.; Veber, A.; Gin, S.; Li, H., Effect of thermally induced structural disorder on the chemical durability of International Simple Glass. *npj Mater. Degrad.* **2018,** *2* (1), 1-11.
39. Greene, R. G.; Ishikawa, T.; Akarapu, R. K. In *P-66: Low Coefficient of Thermal Expansion (CTE) Display Glass Minimizes Chip on Glass (COG) Light Leakage (LL) from Chip Warp*, SID Symposium Digest of Technical Papers, Wiley Online Library: 2019; pp 1481-1484.
40. Jedamzik, R.; Döhring, T.; Johansson, T.; Hartmann, P.; Westerhoff, T. In *CTE characterization of ZERODUR® for the ELT century*, Optical Materials and Structures Technologies IV, International Society for Optics and Photonics: 2009; p 742504.
41. Krohn, M. H.; Hellmann, J. R.; Mahieu, B.; Pantano, C. G., Effect of tin-oxide on the physical properties of soda-lime–silica glass. *J. Non-Cryst. Solids* **2005,** *351* (6-7), 455-465.
42. Keilmann, F.; Hillenbrand, R., Near-field microscopy by elastic light scattering from a tip. *Philos. Trans. R. Soc. A* **2004,** *362* (1817), 787-805.
43. Yeo, B.-S.; Stadler, J.; Schmid, T.; Zenobi, R.; Zhang, W., Tip-enhanced Raman Spectroscopy–Its status, challenges and future directions. *Chem. Phys. Lett.* **2009,** *472* (1-3), 1-13.
44. Lahiri, B.; Holland, G.; Centrone, A., Chemical imaging beyond the diffraction limit: experimental validation of the PTIR technique. *Small* **2013,** *9* (3), 439-445.
45. Ma, X.; Beltran, V.; Ramer, G.; Pavlidis, G.; Parkinson, D. Y.; Thoury, M.; Meldrum, T.; Centrone, A.; Berrie, B. H., Revealing the Distribution of Metal Carboxylates in Oil Paint from the Micro-to Nanoscale. *Angew. Chem.* **2019,** *131* (34), 11778-11782.
46. Dou, T.; Li, Z.; Zhang, J.; Evilevitch, A.; Kurouski, D., Nanoscale structural characterization of individual viral particles using atomic force microscopy infrared spectroscopy (AFM-IR) and tip-enhanced raman spectroscopy (TERS). *Anal. Chem.* **2020,** *92* (16), 11297-11304.
47. Rizevsky, S.; Kurouski, D., Nanoscale Structural Organization of Insulin Fibril Polymorphs Revealed by Atomic Force Microscopy–Infrared Spectroscopy (AFM-IR). *ChemBioChem* **2020,** *21* (4), 481-485.
48. Dazzi, A.; Saunier, J.; Kjoller, K.; Yagoubi, N., Resonance enhanced AFM-IR: A new powerful way to characterize blooming on polymers used in medical devices. *Int. J. Pharm.* **2015,** *484* (1-2), 109-114.
49. Varner, J.; Oel, H. J., Surface defects: their origin, characterization and effects on strength. *J. Non-Cryst. Solids* **1975,** *19*, 321-333.
50. Surdyka, N. D.; Pantano, C. G.; Kim, S. H., Environmental effects on initiation and propagation of surface defects on silicate glasses: scratch and fracture toughness study. *Appl. Phys. A* **2014,** *116* (2), 519-528.
51. Kurkjian, C. R.; Gupta, P. K.; Brow, R. K., The strength of silicate glasses: what do we know, what do we need to know? *Int. J. Appl. Glass Sci.* **2010,** *1* (1), 27-37.
52. Luo, J.; Huynh, H.; Pantano, C. G.; Kim, S. H., Hydrothermal reactions of soda lime silica glass–Revealing subsurface damage and alteration of mechanical properties and chemical structure of glass surfaces. *J. Non-Cryst. Solids* **2016,** *452*, 93-101.
53. Mathurin, J.; Deniset-Besseau, A.; Dazzi, A., Advanced Infrared Nanospectroscopy Using Photothermal Induced Resonance Technique, AFMIR: New Approach Using Tapping Mode. *Acta Phys. Pol. A* **2020,** *137* (1).
54. Li, C.; Zhang, L.; Sun, L.; Wu, C.; Duan, D.; Lin, Q.; Ding, J.; Jiang, Z., A finite element study on the effects of densification on fused silica under indentation. *Ceram. Int.* **2020,** *46* (17), 26861-26870.

55. Suzuki, K.; Benino, Y.; Fujiwara, T.; Komatsu, T., Densification energy during nanoindentation of silica glass. *J. Am. Ceram. Soc.* **2002,** *85* (12), 3102-3104.
56. Gadelrab, K.; Bonilla, F.; Chiesa, M., Densification modeling of fused silica under nanoindentation. *J. Non-Cryst. Solids* **2012,** *358* (2), 392-398.
57. Luo, J.; Zhou, Y.; Milner, S. T.; Pantano, C. G.; Kim, S. H., Molecular dynamics study of correlations between IR peak position and bond parameters of silica and silicate glasses: Effects of temperature and stress. *J. Am. Ceram. Soc.* **2018,** *101* (1), 178-188.
58. He, H.; Hahn, S. H.; Yu, J.; Qiao, Q.; van Duin, A. C.; Kim, S. H., Friction-induced subsurface densification of glass at contact stress far below indentation damage threshold. *Acta Mater.* **2020,** *189*, 166-173.
59. Niu, Y.-F.; Han, K.; Guin, J.-P., Locally Enhanced Dissolution Rate as a Probe for Nanocontact-Induced Densification in Oxide Glasses. *Langmuir* **2012,** *28*, 10733−10740.
60. Gin, S.; Guo, X.; Delaye, J.-M.; Angeli, F.; Damodaran, K.; Testud, V.; Du, J.; Kerisit, S.; Kim, S. H., Insights into the mechanisms controlling the residual corrosion rate of borosilicate glasses. *npj Mater. Degrad.* **2020,** *4* (1), 1-9.
61. Lombardo, T.; Loisel, C.; Gentaz, L.; Chabas, A.; Verita, M.; Pallot-Frossard, I., Long term assessment of atmospheric decay of stained glass windows. *Corros. Eng. Sci. Technol.* **2010,** *45* (5), 420-424.
62. Kenkel, S.; Mittal, A.; Mittal, S.; Bhargava, R., Probe–sample interaction-independent atomic force microscopy–infrared spectroscopy: toward robust nanoscale compositional mapping. *Anal. Chem.* **2018,** *90* (15), 8845-8855.
63. Shao, G.; Wu, X.; Kong, Y.; Cui, S.; Shen, X.; Jiao, C.; Jiao, J., Thermal shock behavior and infrared radiation property of integrative insulations consisting of MoSi2/borosilicate glass coating and fibrous ZrO2 ceramic substrate. *Surf. Coat. Technol.* **2015,** *270*, 154-163.
64. Collin, M.; Fournier, M.; Frugier, P.; Charpentier, T.; Moskura, M.; Deng, L.; Ren, M.; Du, J.; Gin, S., Structure of International Simple Glass and properties of passivating layer formed in circumneutral pH conditions. *npj Mater. Degrad.* **2018,** *2* (1), 4.
65. Kirk, C., Quantitative analysis of the effect of disorder-induced mode coupling on infrared absorption in silica. *Phys. Rev. B* **1988,** *38* (2), 1255.

For Table of Contents Only

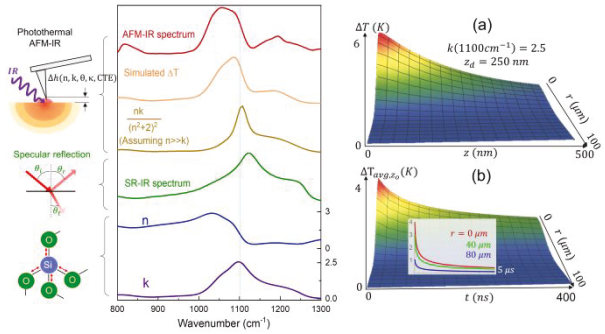

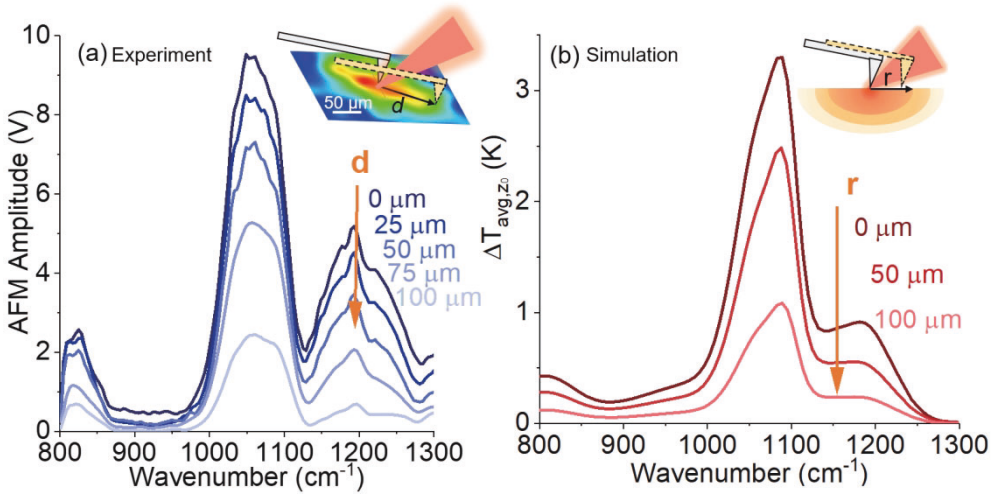

Figure 4. (a) AFM-IR spectra of fused quartz collected at locations with varying distances from the laser focal point. The inset image with a color scale shows the AFM-IR amplitude change over a 200 μm × 200 μm area. The AFM probe is displaced by the distance shown in the figure (d1) along the IR irradiation direction. (b) Local average temperature, ΔT_avg (r,t_p), inside fused quartz as a function of IR wavenumber at r = 0 nm, 50 μm, and 100 μm at a 70o incidence angle. The IR pulse power in the calculation is 2 mW, which is the average power of IR laser pulses also used in the experiment. The calculation results for 50o and 60o incidence angles are shown in Figure S1b.

1400x704mm (600 x 600 DPI)

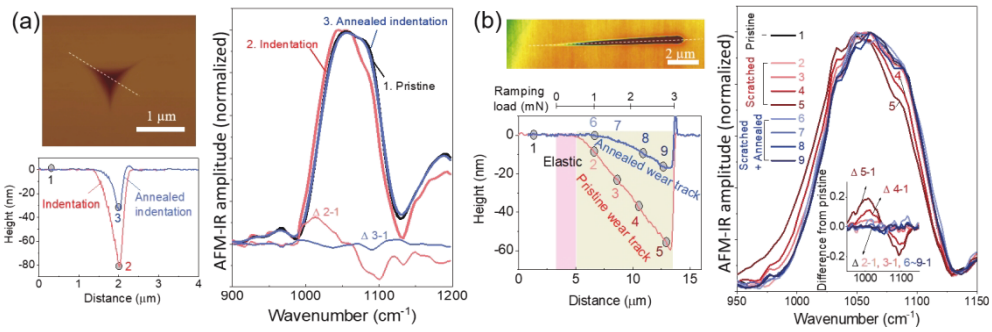

Figure 7. (a) Topography, line profile, and AFM-IR spectra of a nanoindent on fused quartz made with a Berkovich indenter at a 5 mN load. (b) Topography, line profile, and AFM-IR spectra of a nanoscratch on fussed quartz made with a conospherical tip (radius = 150 nm) at a ramp load from 0 mN to 3 mN while sliding over a 10 μm distance. The same samples were analyzed before and after sub-Tg annealing. The differences (△) between local spectra are also shown.

1457x470mm (600 x 600 DPI)